In-situ detection of redeposited spatter and its influence on the formation of internal flaws in laser powder bed fusion

Additive Manufacturing 47 (2021) 102370

Contents lists available at ScienceDirect

Additive Manufacturing

journal homepage: www.elsevier.com/locate/addma

Research Paper

In-situ detection of redeposited spatter and its influence on the formation of internal flaws in laser powder bed fusion

Claudia Schwerz *, Ahmad Raza, Xiangyu Lei, Lars Nyborg, Eduard Hryha, Håkan Wirdelius

Chalmers University of Technology, Department of Industrial and Material Science, Sweden

ARTICLE INFO

Keywords:
Spatter redeposition
In-situ monitoring
Lack of fusion
Flaw detection
Defects

ABSTRACT

The pervasive adoption of laser powder bed fusion (LPBF) as an industrial manufacturing technique relies on the improvement of its repeatability, currently limited by the stochastic formation of flaws. Considering that large flaws can form randomly and despite the optimization of process parameters, an in-situ monitoring technique suitable for detecting deviations that originate these critical flaws is paramount. The redeposition of spatters on the build area has previously been identified as one of the factors responsible for the rise of internal flaws, but so far limited are the efforts towards their detection. This study aims to detect spatter redeposits via in-situ monitoring and to couple the detections to lack of fusion. For that, long-exposure near-infrared in-situ monitoring associated with image analysis is employed to determine the exact locations and quantify the incidence of spatter redeposits across three full builds performed at varying layer thicknesses. The existence and distribution of internal flaws is verified ex-situ by means of ultrasonic inspection and metallography. The formation of internal flaws is attributed to spatter redeposits after detailed characterization of size, particle and surface morphology of spatter and identification of particles with identical characteristics on the fracture surface in the adjacencies of lack of fusion. It is found that spatters preferentially redeposit on the adjacencies of the gas outlet, but that the affected portion of the build area and the prevalence of detections is heavily dependent on the powder layer thickness employed in the manufacturing process. The monitoring system setup preferentially acquires signal from spatters redeposited on print regions, making it particularly suitable for flaw detection.

1. Introduction

Lack of repeatability of laser powder bed fusion (LPBF) manufactured material is reported as one of the main barriers to its widespread adoption, particularly by industrial sectors where defect avoidance is crucial [1]. LPBF-processed material is susceptible to flaws even when optimized process parameters are utilized [2,3]. Spatters, process byproducts whose formation is inherent to the process, have been reported as one of the primary sources of stochastic flaws[1] [3].

Spatters can consist of ejections of molten material from the melt pool due to recoil pressure [4,5], typically with size 25–100 μm [6]. The ejecta can collide and merge, resulting in even larger particles [6]. Particles entrained by the low-pressure zone created by the vapor jet can interact with the laser beam and be ejected as hot spatters [6] or coalesce and be subsequently melted [7], resulting in sizeable incandescent ejecta. The suddenly unstable interaction between laser and part that arises when the melt pool comes in contact with a pre-existing large flaw can also cause the formation of hot spatter [8]. Cold spatters consist of particles initially present on the powder bed that are scattered due to the impact of metallic vapor [4] or entrained by the low-pressure zone then directly ejected prior to interaction with the laser beam [6].

Spatters can be much larger than the powder feedstock [9–11]; hence, when redeposited on the powder bed, the local increase of layer thickness can hinder the complete melting of the powder layer [12] and attenuate the laser beam [2], potentially resulting in insufficient melting. Nassar et al. [13] observed that melt pool ejecta perturb melt pool geometry and argued these disturbances are a potential cause of lack-of-fusion. Moreover, spatters selectively oxidize, particularly in case the alloy contains elements with elevated oxygen affinity, resulting in surface oxide layers of thickness up to several micrometers [9] that form internal flaws and degrade mechanical properties [14].

Due to the stochastic nature of spatter-induced flaws, in-situ

* Correspondence to: Department of Industrial and Material Science, Chalmers University of Technology, Rännvägen 2, SE-412 96, Gothenburg, Sweden.
E-mail address: claudia.schwerz@chalmers.se (C. Schwerz).

[1] The term "flaw" is employed in this paper to refer to pores and lack of fusion, as in engineering and inspection contexts the term "defect" refers to flaws that affect the fitness for service of a component [32].

https://doi.org/10.1016/j.addma.2021.102370
Received 9 July 2021; Received in revised form 10 September 2021; Accepted 27 September 2021
Available online 2 October 2021

detection of spatter redeposits is paramount for understanding the general behavior, from a research perspective, and monitoring deviations that indicate flaw formation, from a manufacturing perspective. In-situ monitoring of spatter has mainly been used to elucidate the formation mechanisms utilizing high speed [4,6,7] and X-ray imaging [15,16]. Repossini et al. [17] and Zhang et al. [18] have used in-situ monitoring of spatter aiming the assessment of process quality. By processing the signal obtained from high-speed imaging, multiple descriptors of the ejecta are collected and correlated to both desirable and sub-optimal process conditions. However, since spatters give rise to internal flaws specifically after landing on the regions of the powder bed to be exposed by the laser beam, a suitable technique for monitoring spatter redeposits is crucial for monitoring focused on flaw detection.

This study aims to detect redeposited spatter, assess its distribution in the build chamber, and determine its influence on the formation of internal flaws in multilayer builds. For that, three relatively densely packed builds are printed with optimized process parameters and monitored with long-exposure imaging, a technique deemed suitable for signal acquisition of redeposited spatter. The output of in-situ monitoring is processed to detect spatter redeposits on the build area on each layer of each build. The printed parts are evaluated in terms of flaw distribution, both non-destructively and destructively and correspondences between lack of fusion flaws and detected spatter redeposits are established.

2. Methods

The experiments were conducted in an EOS M290 (EOS GmbH Electro Optical Systems) LPBF machine in argon atmosphere with oxygen content lower than 0.1%. A Yb-fiber laser of maximum nominal power of 400 W and spot size of 100 μm is utilized. The feedstock material is gas atomized Hastelloy X powder with composition compliant with UNS N06002 and particle size distribution 19 μm (d10), 35 μm (d50) and 58 μm (d90). The three builds in this study were composed of parts with constant cross-section (top view in Fig. 1A) manufactured using nominal layer thicknesses of 80 μm, 120 μm and 150 μm. These values were selected to assess the potential for productivity increase of the LPBF process with particular reference to layer thickness. The build was designed so the laser exposed area is large enough to generate enough process byproducts and to fill the build plate area to verify the effect of such byproducts spatially. The employed process parameters have been previously optimized for the attainment of fully dense material and consist namely of laser power of 370 W, scan speed of 900 mm/s, hatch spacing of 100 μm. Exposure order against the gas flow direction was employed. Gas flow settings were kept constant throughout the builds.

After the completion of each build, spatter samples were collected from the top of the extraction nozzle, located by the gas outlet. These samples, as well as a sample of the feedstock powder, were characterized in terms of surface morphology and chemistry. High-resolution scanning electron microscopy (HR SEM) with a LEO Gemini 1550 was conducted to evaluate the variation in surface morphology from feedstock powder to collected spatter. To identify the change in elements and their chemical state from the surface of feedstock powder to spatter powder, X-ray photoelectron spectroscopy (XPS) (ULVAC-PHI 5500) was used. Powder samples for XPS analysis were mounted on 3 M carbon tape, and the dimensions of the analysis area were 300 μm × 300 μm. Due to the large measurement area, XPS results represent a statistical average of 20–30 particles. To estimate the oxide layer thickness, Ar^+ ion etching was done with etch rate of 5.2 nm/min. The etch rate was calibrated using TaO_2 foil. The survey spectra and high-resolution narrow scans were acquired using a pass energy of 280 eV and 26 eV, respectively.

The manufacturing process was monitored utilizing the EOS EOSTATE Exposure OT system, consisting of a 5-megapixel sCMOS (scientific complementary metal-oxide-semiconductor) camera positioned on top of the build chamber and comprises the entire build platform area in its field of view. A bandpass filter of 900 nm ± 12.5 nm is placed on the camera to filter detection of reflected laser, with wavelength 1064 nm, of plasma radiation, with wavelength in the range of 400–600 nm, and of visible light, 380–700 nm, to avoid detection of environmental noise. The camera acquires 0.1-s exposure images during the processing of a layer and outputs a single image per layer. Each pixel in the output image assumes the value of maximum intensity of the corresponding acquisition region of size 125 μm × 125 μm. A more detailed description of the system can be found in [19].

A detector is constructed to determine the existence and location of spatter redeposits in every image acquired by the monitoring system. A Laplacian of Gaussian (LoG) operator, expressed in (1), is convolved with the image $I(x,y)$ for blob detection [20]. Since the convolution operation is associative, the application of the LoG filter is equivalent to a two-step convolution, in which the Gaussian step attenuates noise, while the Laplacian is a measure of the second derivative of the smoothed image and highlights regions of rapid intensity change [21]. The standard deviation σ is selected so the filtered image converges to local extrema upon detection of a spatter redeposit. Due to the homogeneous size of the features in relation to the image resolution (the typical spatter size is in the order of 100 μm and the image resolution is 125 μm per pixel), detections were performed at a single scale. After filtering, non-minimum suppression was applied to ensure unique detections in each spatter.

$$LoG(x,y) = -\frac{1}{\pi\sigma^4}\left[1-\frac{x^2+y^2}{2\sigma^2}\right] \quad \exp(-\frac{x^2+y^2}{2\sigma^2}) \tag{1}$$

Ex-situ ultrasonic inspection was performed in the form of linear scan transversally to the build direction. By using a 64-elements linear phased array longitudinal-wave-probe (Zetec LM-5 MHz), the linear scanning was performed on each specimen with the probe fixed at a single position. The ultrasonic waves were emitted from an aperture of 16 elements of the probe and propagated into the build with 0-degree refraction angle. Proper delay laws were applied to realize the beam focusing at one scan position. To cover the entire region of each specimen, the aperture travels along the whole array with a step of 1 element. The ultrasonic inspection data were collected and recorded under a sampling frequency of 100 MHz by a corresponding data acquisition hardware unit labeled TOPAZ64 from Zetec, and then post-possessed using UltraVision software. The longitudinal wave speed in Hastelloy X is about 5700 m/s. Using the phased array probe with center frequency of 5 MHz, the wavelength in this material is about 1.1 mm, which results in sensitivity of approximately 500 μm [22].

3. Results

3.1. Distribution of spatter on the build area

A long-exposure image of each build layer is acquired with the goal of monitoring and detecting disturbances in the process, particularly redeposited spatters. A sample image representative of a single layer can be observed in Fig. 1A. Some artifacts are noticeable across the entire build area, particularly stripes, which reflect the scan strategy employed combined with the system's acquisition gaps. The long-exposure images revealed deviations in the form of high-intensity spots preferentially distributed towards the gas outlet (Fig. 1C). Due to this consistent spatial distribution, these indications are likely the manifestation of spatter redeposition on the powder bed.

Aiming to automate the detection[2] of these features, a spatter detector was constructed with Laplacian of Gaussian filtering followed by identification of the local minima. A sample output of the detection

[2] The term "detection" is employed as used in image analysis contexts, i.e., referring to the determination of the presence and location of an object of interest.

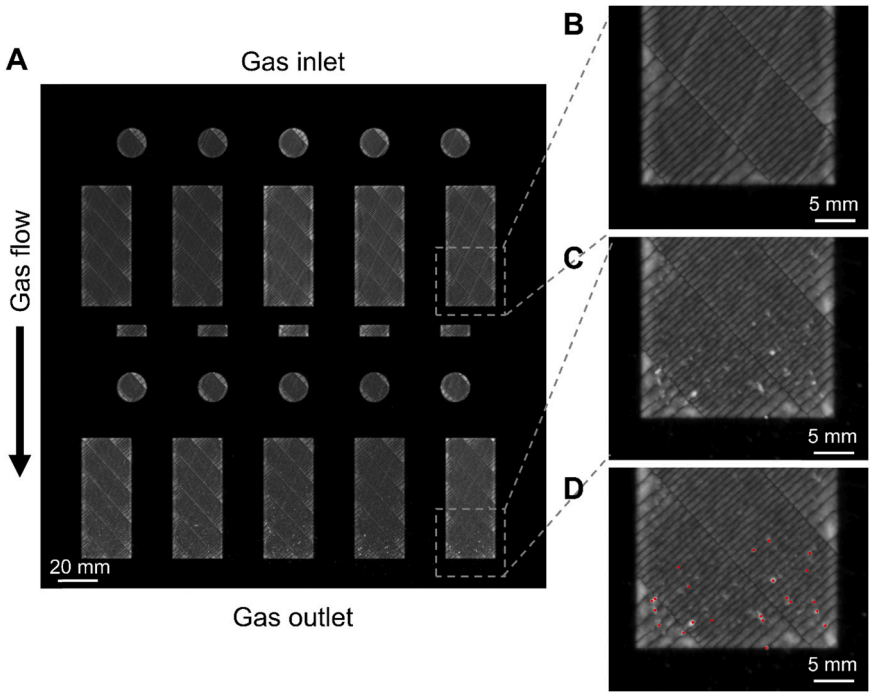

Fig. 1. Sample output from the monitoring system (EOS EOSTATE Exposure OT) and from the spatter detection algorithm. (A) Sample long-exposure image consisting of the signals emitted during the exposure of a single layer on the entire build area. Areas with disturbances are observed preferentially near the gas outlet (C). A sample area without any identified disturbances is highlighted for comparison (B). A sample output from the spatter detection algorithm (D).

algorithm is visualized in Fig. 1D, in which the region shown in Fig. 1C is overlayed with detections. The detected redeposited spatters are preferentially located on laser-exposed regions, even though the spatters land equally on laser-exposed and unexposed regions of the powder bed. This observation illustrates the increased heat flow rate from the spatter to the powder bed in relation to the heat flow rate from spatters to the printed area, as the camera employed captures long-exposure infrared emissions. The difference in the heat flow is due to the elevated temperature on the printed area, which decreases the cooling rate of spatter particles, thereby generating an intensity peak on the monitored signal.

Images obtained by in-situ monitoring of a specimen in two distinct layers are presented in Fig. 2A and C. The same images saturated to enhance the contrast outside part boundaries show the overall trajectory of the spatter particles (Fig. 2B and D, respectively). The initial trajectory is parallel to the scan lines, agreeing with the high-speed camera observations made by Bidare et al. [7] and then aligns to the direction of the gas flow. The orientation of the stripes in a stripe scanning strategy affects the spatial distribution of the redeposited spatter. In Fig. 2B, the particles ejected with an initial velocity vector with a component in the $-x$ direction are also partly ejected against the gas flow ($-y$ direction), therefore tend to be removed less effectively from the build area than the particles partly ejected in the $+x$ direction, that are ejected in the same direction as the gas flow ($+y$). The initial momentum towards $-x$ combined with the less effective removal from the build area results in preferential deposition of the particles on the left side of the build plate. Conversely, the stripe orientation in Fig. 2C leads to less effective removal of ejecta initially traveling in the direction of $+x$, which in its turn results in preferential accumulation of spatter on the right side of the build plate. The discrepancy in the spatial distribution of detections can be observed in Fig. 2E. Stripe rotation homogenizes the distribution of spatters transversally to the direction of gas flow along the build.

3.2. Influence of layer thickness on the prevalence of redeposited spatters

Three builds containing the same specimens and layout were performed under the identical experimental conditions and parameters,

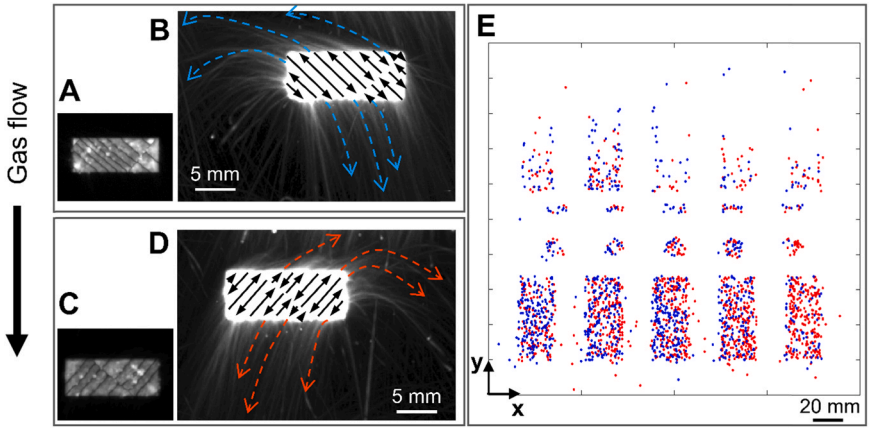

Fig. 2. Distribution of redeposited spatter on the build area depending on stripe orientation. The raw signals (A) and (C) show the stripe orientation, schematized on the corresponding image with enhanced contrast outside part boundaries (B) and (D). The schematized images also show the trajectory of spatters. The resulting detections of spatter redeposits on the layer with stripe orientation as (A) are represented in blue, while the detections stemming from stripe orientation as (B) are represented in red (E).

except for the nominal layer thickness, which assumed the values of 80 μm, 120 μm and 150 μm in the different builds. Application of the spatter detector in the long-exposure images of these builds reveals a larger amount of spatter redepositions on the build area as the thickness of the powder layer increases (Fig. 3D–F). In the build where nominal layer thickness of 80 μm was employed, the number of detections per layer averages 1, and the maximum number of detections on a layer is 9, indicating that this build is not particularly affected by spatter redeposition. In the builds where a significant amount of spatter redeposits was identified, relatively few detections are present in low build heights, indicating that spatter redeposition becomes substantial only after deposition of the first layers. The incidence of spatter with increasing build heights diverges for the two builds, which is indicative of the randomness of the phenomenon, that is presumably affected by other stochastic events occurring in the build process, for example fluctuations in the gas flow. In the build performed with layer thickness 120 μm, the number of detections increases with the build height, while in the build performed with layer thickness 150 μm, the number of spatter detections spike at different build heights (Fig. 3F).

The redeposition occurs preferentially close to the gas outlet in all cases. However, redeposited spatters are detected further away from the gas outlet as the layer thickness is increased (Fig. 3A–C). These observations show that the spatters are removed less effectively and affect a higher extension of the build area when higher layer thicknesses are employed in manufacturing.

3.3. Characterization of spatter and feedstock powder

Feedstock powder and spatter particles collected from each build were analyzed regarding particle size distribution, surface morphology and surface chemistry. Particle size distributions were obtained from analysis of SEM images. At least 350 particles were measured for each powder sample. Fig. 4A presents spatter size distribution in the form of density plots, in which the area under the curve equals one. The spatter collected from all three builds has a bimodal size distribution, with peaks located around 30 μm and 90 μm. The largest spatter identified is about 200 μm diameter for all builds. Fig. 4B shows the particle size distribution of the feedstock powder for reference. Since the particle size distribution (PSD) measurement hereby performed is based on particle count rather than on weight or volumetric basis, the shape of the curve diverges that obtained through laser diffraction [23].

Most spatter particles have a spherical shape (Fig. 5A), representing either remelting and solidification during the time of flight or scattering of particles initially present on the powder bed. Some of the largest particles identified are agglomerates of either particles in the size range of the feedstock (Fig. 5B), of large melt ejecta (Fig. 5D), or a combination of both (Fig. 5C), illustrating different spatter formation mechanisms.

The surface morphology of feedstock powder is illustrated in Fig. 6A. The surface of the particle is rather clean and does not show any sign of oxide particulate formation. Contrarily, spatter collected from gas outlet shows that most of the particles are relatively coarser than feedstock powder with a few fine spatter particles (see Fig. 6B). The surface morphology of all the spatter particles is distinguishably different from feedstock powder and lacks dendritic structure. Smaller particles have extremely oxidized surfaces with small oxide particulate formation over the surface stemmed from high surface energy. Larger particles have slightly different oxidizing tendencies, with some particles forming large dark oxide particulates and others forming a random morphological oxide pattern. In summary, the generated particles have both coarser size and highly oxidized surface compare to the feedstock powder. Comparison of spatters from each build has not shown a significant difference in size, particle or surface morphology, indicating that the main difference among builds is the number of spatter particles generated.

To further characterize the change in surface chemistry from feedstock powder to spatter powder, XPS analysis was conducted. XPS survey spectra measured on the as-received surface of feedstock and spatter powders are compared in Fig. 7. In spectra from feedstock powder, distinctive peaks from nickel ($Ni2p_{3/2}$) at ~853 eV, iron ($Fe2p_{3/2}$) at ~710 eV, chromium ($Cr2p_{3/2}$) ~575 eV, molybdenum ($Mo3d_{5/2}$) at ~280 eV, silicon (Si2p) ~100 eV, carbon (C1s) ~284.8 eV and oxygen (O1s) at ~531 eV can be observed. Survey spectra from spatter powders are significantly different from feedstock powder, where additional aluminum (Al2p) and titanium ($Ti2p_{3/2}$) peaks are appearing at ~74 eV and ~458 eV. Though the contents of Al and Ti (< 0.15at.%) are very low in the alloy, higher susceptibility for oxidation is driving it to the

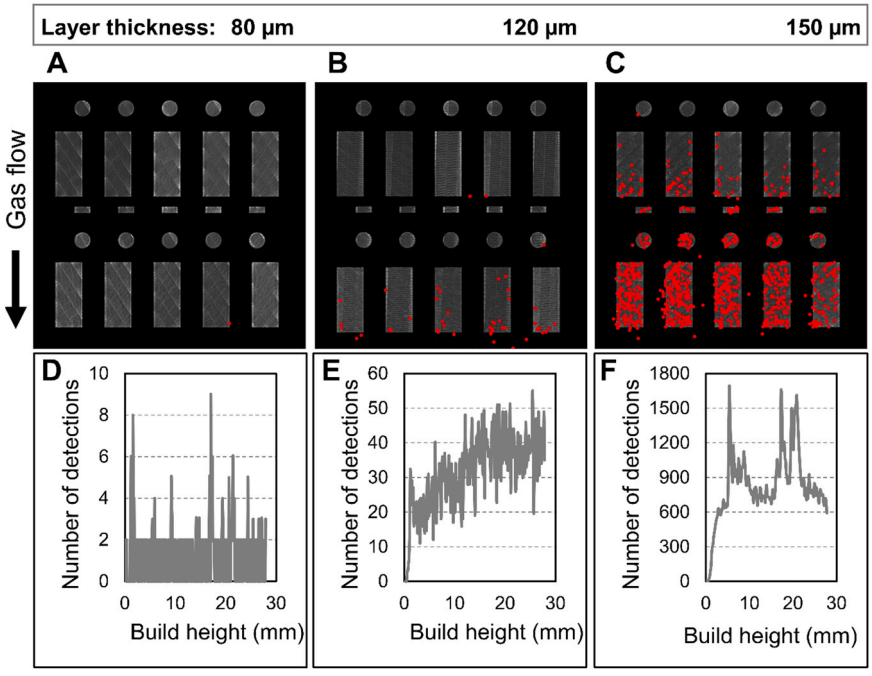

Fig. 3. Incidence of redeposited spatters in builds with varying layer thicknesses. Sample detections on builds with layer thickness 80 μm (A), 120 μm (B) and 150 μm (C). The number of detections per layer versus build height are presented in D–F.

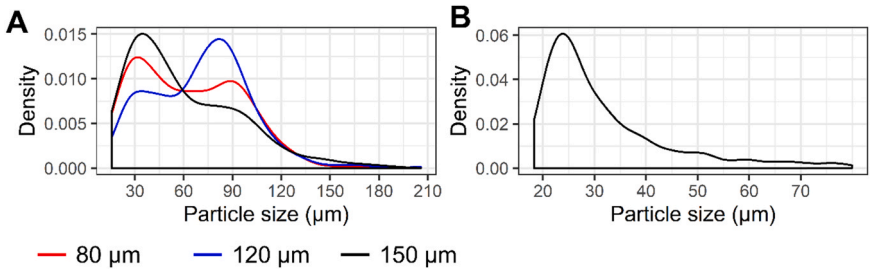

Fig. 4. Particle size distribution of spatter (A) and feedstock powder (B), based on the particle count. The layer thickness employed in the build from which spatter was sampled is indicated.

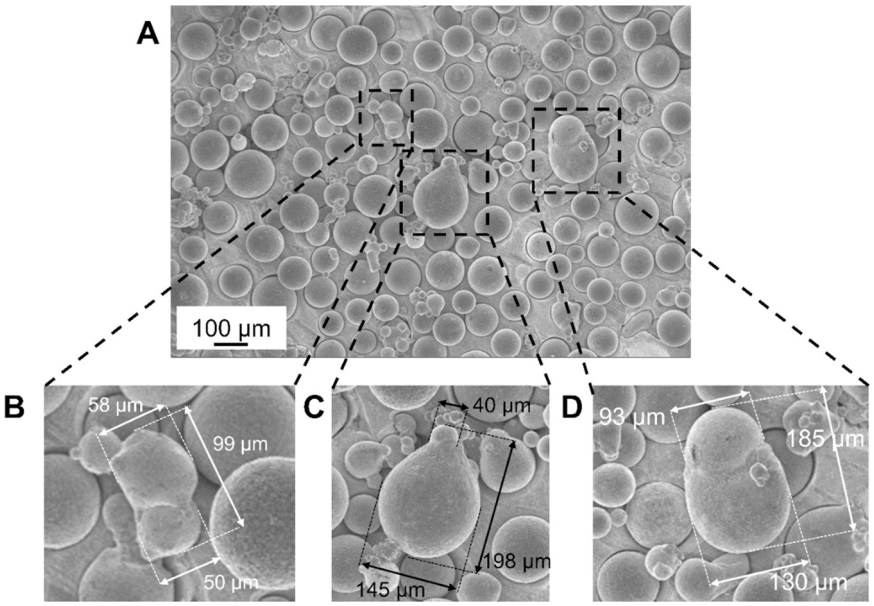

Fig. 5. Morphology of spatter particles. A representative sample is shown in A. In B, C and D, some of the largest agglomerates in this sample are highlighted and measured.

surface to form Al and Ti-based oxide. The relative intensity of all other metallic elements (Ni, Fe, Mo) is substantially decreased except Cr. The relative intensity of Cr2p is significantly increased in the spatter powders, indicating the preferential oxidation of Cr due to its high affinity for oxidation. The comparison of survey spectra of spatter samples collected from different builds with varying layer thickness does not show a significant difference. Hence, it is concluded that the spatter particles generated in different build cycles have similar surface chemistry where the surface is covered with Cr- and Ti-based oxides.

To investigate the extent of oxidation observed in survey spectra, it is important to determine the average oxide layer thickness on the powder surface. The thickness of oxide layer is determined by using the narrow scan of Ni2p spectra utilizing the methodology developed in Ref. [24]. This method is particularly designed for spherical surfaces to rule out any shadowing effect [25]. A relationship between the intensity of $Ni2p^{met}$ and etch depth is used to determine the oxide layer thickness. The thickness where the intensity of $Ni2p^{met}$ reaches 65% of highest intensity of $Ni2p^{met}$ is considered as the thickness of the oxide layer. Here, a comparison of the oxide layer thickness of feedstock powder and collected spatter particles from build with layer thickness of 150 μm is presented in Fig. 8B. The feedstock powder, which showed comparatively a clean surface, has oxide layer thickness of 3 nm, see Fig. 8A. This thickness is resulted from a protective oxide layer formation on the powder surface and presence of random oxidized particles in the feedstock powder as it was not virgin powder. On the other hand, the analysis of spatter powder elucidates the formation of a thick oxide layer of ~76 nm. This result is confirming the oxide nature of particulates observed in the SEM analysis on spatter powder surface.

3.4. Correspondence between redeposited spatter and internal flaws

To determine the correlation between detected redeposited spatter and internal flaws, both destructive and non-destructive testing were utilized. Metallographic analysis performed in cross-sections of specimens in which monitoring and detection indicated pervasiveness of spatter redeposits (Fig. 9D) revealed large internal flaws (Fig. 9E). These internal flaws are located inter melt pool boundaries, i.e., are lack of fusion flaws, and are observed in conjunction with round particles with dendritic structure, indicated by white arrows in Fig. 9F and G. In contrast, in specimens with low prevalence of spatter redeposits (Fig. 9B), no major internal flaws are identified (Fig. 9C). As the process parameters employed in the manufacturing of these specimens are identical, the flaws observed are attributed to the presence of spatter redeposits.

To verify the correspondence between spatter detections and internal flaws volumetrically, ultrasonic inspection was performed in the specimens with large rectangular cross-sections in Fig. 1A. Fig. 10 shows the inspection results in the form of pseudocolor maps that represent the reflected wave energies from a side-view perspective of the specimens (i.e., ultrasonic B-scans). All figures are reinforced with an energy gain of 30 dB as the original signals were too weak to be visible. Regions represented with colors corresponding to the upper end of the scale indicate

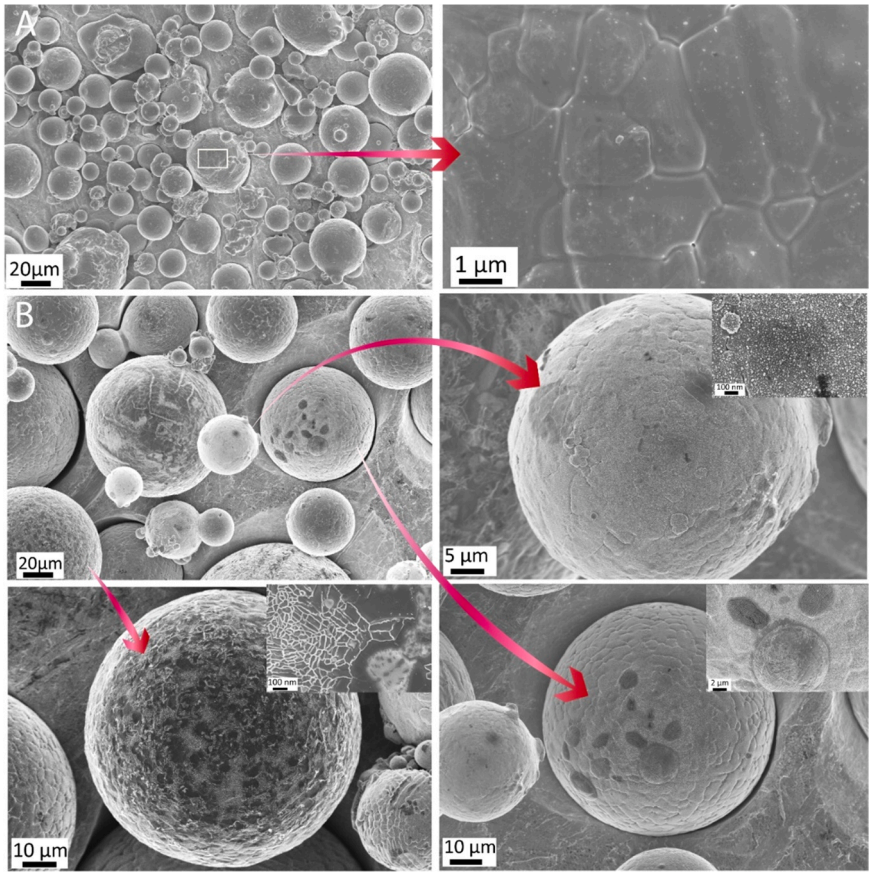

Fig. 6. SEM analysis with focus on surface morphology of feedstock powder (A) and spatter particles obtained at 150 µm layer thickness (B) with higher magnification inserts of different particles highlighted by red arrows.

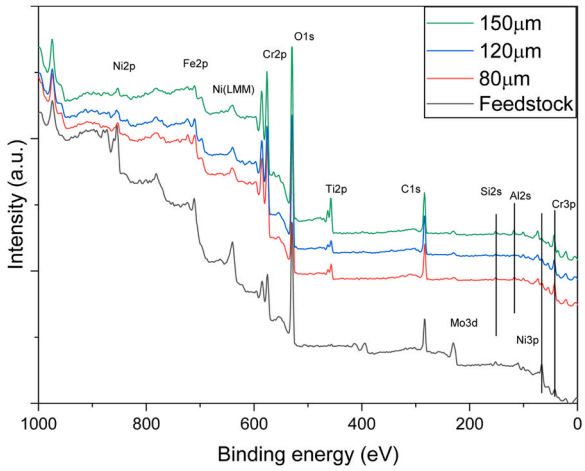

Fig. 7. Comparison of XPS survey spectra from feedstock powder and spatter samples collected from the build with layer thickness of 80 µm, 120 µm, and 150 µm.

reflected waves of higher energy presence of discontinuities. Regions represented with colors in the lower end of the scale indicate reflected waves of lower energy and correspond to features such as inhomogeneous grain structures. Fig. 10A shows the inspection result of a specimen built with layer thickness of 150 µm in the adjacencies of the gas outlet. Multiple indications of flaws larger than 500 µm are present and located preferentially at build heights of 5 mm, 17 mm and 19 mm, which correspond to the peaks in detection of spatter redeposits for this build (Fig. 3F). Even though typically a low number of spatter redeposits are detected by in-situ monitoring in the region close to the gas inlet, at the build height 19 mm, a large number of detections is made in this area. The ultrasonic inspection represented in Fig. 10B indicates consistent results, as large internal flaws are detected at this build height even in the specimens located near the gas inlet. A few indications of flaws are present in specimens built with layer thickness 120 µm close to the gas outlet (Fig. 10C), in the region closest to the gas outlet, agreeing with the location of detected spatter redeposits in Fig. 3B. In the remaining specimens (Fig. 10D–F), no indications of flaws larger than 500 µm are present, in agreement with the low prevalence of detections in Fig. 3A and B.

Fig. 11A illustrates the presence of a spatter particle with cross-section ~136 µm and the effect of its deposition on solidifying melt pools. The melt pools were sequentially deposited from left to right. The microstructure indicates that the spatter particle landed on a solidifying melt pool and incited competing solidification fronts on the melt pool. The bonding between particle and bulk material is incomplete in this region, resulting in a sharp discontinuity. The energy input from the neighboring scanning track is sufficient to partially fuse the particle and incorporate it to the next melt pool. Similar microstructure can be identified in the immediacies of internal lack of fusion flaws. In Fig. 11B, lack of fusion is observed on the interface of a dendritic region characteristic of spatter and a region with radially disposed laths. The lack of fusion is laterally limited by the boundaries of two melt pools that partially fused the spatter and the lath region. Fig. 11A also illustrates how particles significantly larger than the nominal layer thickness are incorporated in the material despite recoating.

More often, rounded particles with dendritic structure are observed in the surroundings of large internal lack of fusion, as observed in Fig. 9F and G and in Ref. [13]. It is not trivial to determine whether these features are spatter, as similar spherical structures can originate due to the

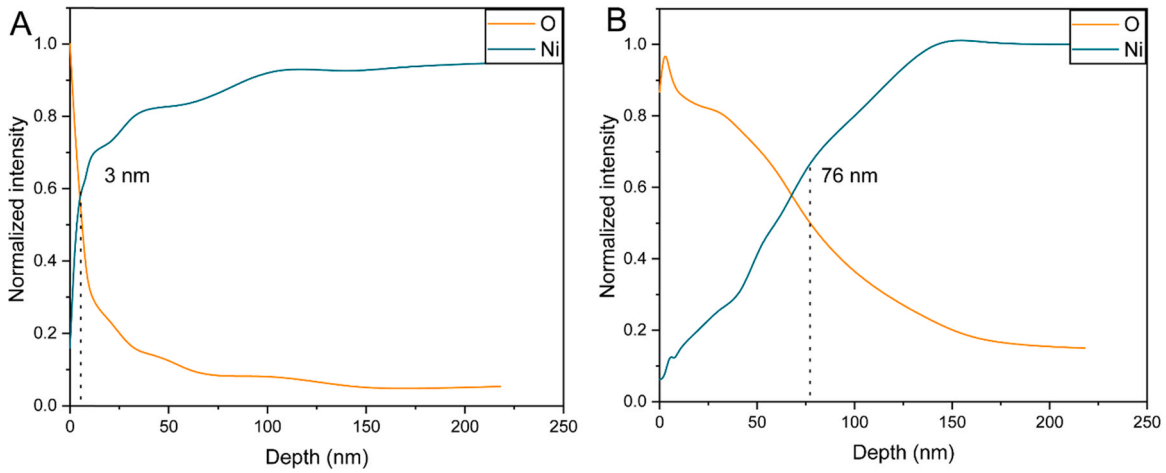

Fig. 8. Oxide layer thickness determination in (A) feedstock powder and (B) spatter sample collected from the build with layer thickness of 150 μm.

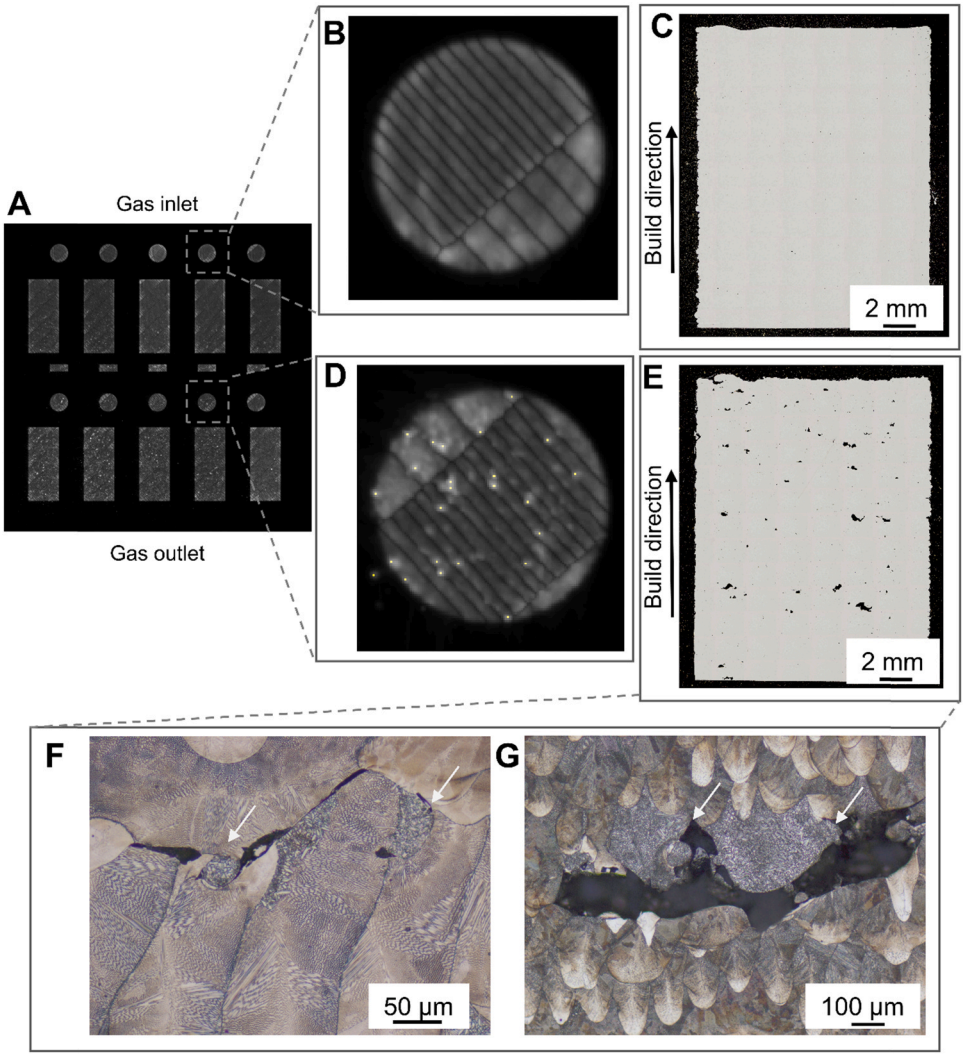

Fig. 9. Correspondence between detections of spatter redeposits and internal flaws. Considering the build layout (A), a low number of spatter redeposits are detected in specimens manufactured in the proximity of the gas inlet (B). Metallographic analysis of these specimens reveals no major internal flaws (C). Detections of spatter redeposits can be abundant in specimens manufactured in the proximity of the gas outlet (D), and these specimens present large internal flaws (E). Round particles with dendritic structure neighbor lack of fusion flaws (F) and (G).

surface tension of the liquid that fails to bond to the substrate [2].

To confirm the connection between lack of fusion defect and spatter particles landed on the samples, fractographic analysis is conducted. A micrograph of fractured surface in a lack of fusion region is shown in Fig. 12A, where multiple small unfused particles can be seen along with a large particle. The size of finer particles is in the same range of feedstock powder, whereas the diameter of the large particle is about 230 μm. In Fig. 12B, higher magnification surface analysis of the large particle surface shows that it is covered with fine oxide particulates, also present in spatter particles. Therefore, it can be assumed that the spatter

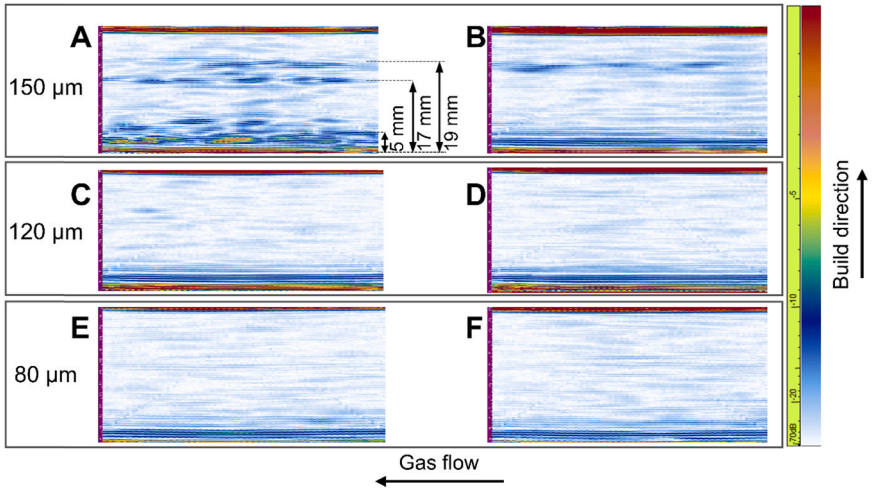

Fig. 10. Results from ultrasound inspection (B-scans) of specimens from builds where layer thickness of 150 µm (A-B), 120 µm (C-D) and 80 µm (E-F) were employed.

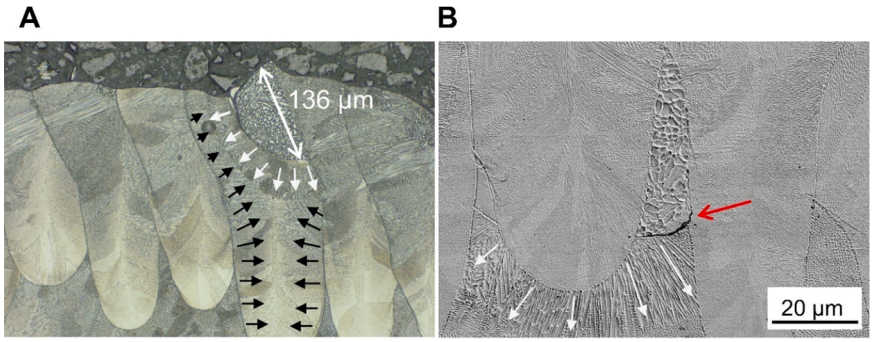

Fig. 11. Interaction mechanism between spatter redeposit and a solidifying melt pool. (A) A spatter particle of cross-section ~136 µm incites a solidification front (schematized with white arrows) that competes with the solidification fronts in the melt pool (schematized with black arrows). (B) The microstructure generated by this interaction is identified in the adjacencies of internal lack of fusion, indicated by a red arrow.

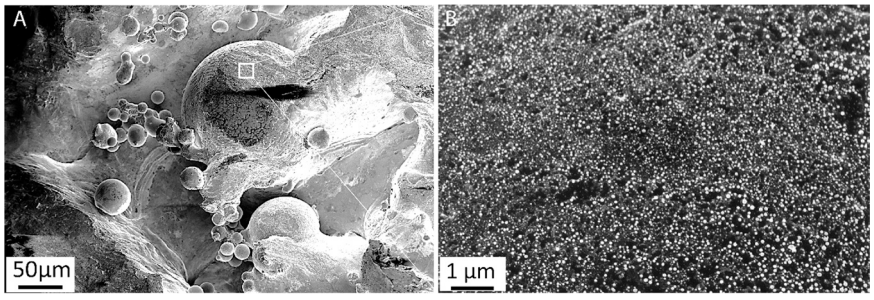

Fig. 12. Fractography micrograph in lack of fusion of zone with high magnification insert of unfused particle surface.

particle was partially fused along with the following layer after redepositing, but not fully melted due to its size and highly oxidized surface. Similar structures are observed in the lack of fusion flaws in Fig. 9F and G. Hence, the correspondence between spatter particle redeposition on build and lack of fusion defect formation can be established based on the similar size and surface morphology of spatter particle and the unfused particle present in lack of fusion zone.

4. Discussion

In this study, three LPBF builds in Hastelloy X were performed with parameters optimized to yield fully dense materials at three distinct layer thicknesses 80 µm, 120 µm and 150 µm. Utilizing a near-infrared long-exposure imaging system and image analysis approaches, redeposited spatters were detected. With that, the distribution of redeposited spatter in the build chamber and its influence on the formation of lack of fusion were determined.

Spatter redeposited on the powder bed interacts with the laser beam in the LPBF process, generating flaws. Thus, a technique suitable to acquire signal emitted from these particles can be used for in-situ monitoring focused on flaw detection. The spectral range of the acquisition system employed in this study enables detection of incandescent spatters, which experience the most oxidation and can have a more important influence on the formation of lack of fusion. The extended shutter time employed enhances the signal gain from static spatters, i.e., spatters that landed on the build area. As depicted in Figure 11A, the

deposition of the spatter particles can occur on a solidifying melt pool. With that, signals from both events are captured simultaneously, thus resulting in higher acquired intensity in relation to separately occurring events. The spatters also land in other regions where a weaker base signal is captured, in which case the signal acquired from particle deposition will also be overlayed with the surrounding base signal, thus resulting in a higher signal at the location of their deposition. The detection method takes this acquisition characteristic into account by basing the decision on whether to categorize the region as spatter or not spatter on the contrast rather than the absolute intensity. Nonetheless, higher contrast and detectability are obtained from the spatters redeposited on areas previously exposed by the laser in comparison to those deposited on the powder bed. Hence, the monitoring system setup preferentially acquires signal from spatters redeposited on regions actively utilized in the manufacturing process, making it particularly suitable for flaw detection.

Earlier studies [2,12] have identified that spatter redeposits preferentially in the adjacencies of the gas outlet. By constructing and employing a spatter detector on long-exposure images, it was also possible to determine the exact locations and quantify the incidence of spatter redeposits. By enhancing the contrast in the regions external to part boundaries, it was possible to observe the general trajectory of spatters and to notice that different spatial distributions of redeposits are possible depending on the laser scan pattern. For example, Anwar and Pham [26] identified a distinct spatial distribution pattern due to unidirectional laser scanning against the direction of gas flow, with spatters redeposited along the gas flow direction preferentially close to the laser-exposed area.

One of the flaw formation mechanisms reported in LPBF is laser beam attenuation, which occurs when process byproducts, including metal condensates of less than 1 μm diameter, absorb and scatter laser energy when in the laser path, resulting in incomplete fusion of the powder particles [27]. This phenomenon can be location-dependent, as decreased gas flow has been measured near the gas outlet [27] and decrease in the pressure causes expansion of the metal vapor in the region where the laser beam interacts with powder and process byproducts, enhancing spatter formation [28]. Whilst flaws in the bulk material were preferentially observed close to the gas outlet, the threshold location to where these flaws exist varies with the amount of spatter generated. This indicates that laser beam attenuation, if not associated with the redeposition of spatter on the powder bed, is not the determining mechanism of flaw generation observed.

The low prevalence of detections in the first layers if the build can be explained by the increase in the effective powder layer thickness and by the emergence of an additional spatter formation mechanism as the build process progresses. Since optimized process parameters are utilized, no large internal flaws exist in the first layers. However, as the build progresses, spatters are formed and redeposit on the surface of the parts being printed, generating large lack of fusion flaws. During the exposure of subsequent layers, the laser interacts with the pre-existing flaws, generating defect-induced spatter [8]. The occurrence of powder agglomerates has also been reported to increase as the build progresses [7].

Previous work had inferred the presence of spatter in the material through observation of increased surface roughness combined with CT scan [12], or confocal microscopy and ultrasonic inspection [2]. The present paper established by direct observation and by using a more mature inspection technique that regions where spatter redeposits are detected contain lack of fusion. Moreover, analysis of the fracture surface established a direct correlation between the presence of lack of fusion and spatter, unequivocally distinguished by its state of oxidation. The spatter generated from Hastelloy X is covered with chromium- and titanium-rich oxide layer of average thickness 76 nm. The particles with oxidized surface not only attenuate the beam, but also require more energy for melting and incorporation in the melt pool and in the bulk material, thereby favoring the formation of lack of fusion flaws. The spatter collected on top of the extraction nozzle by the gas outlet has a bimodal size distribution with peaks around 30 μm and 90 μm. Most spatter particles are round, but some agglomerates are consistently observed as a result collision and merging of melt ejecta [6] and coalescence of entrained particles [7]. As the sampling has been performed on the top of the extractor nozzle, which is raised a few centimeters from the powder bed, mostly particles ejected from the build process are presumably collected. For this reason, the samples obtained are deemed to be representative of spatters formed in the process.

The amount of spatters formed is dependent on the laser exposed area and on the process parameters used. It has previously been demonstrated that more spatter is formed when multiple lasers operate [29] and when the energy input is increased, either by increase of laser power [4,11] or decrease in laser scan speed [30]. The present study, conducted with constant processing conditions, except layer thickness, shows that this process parameter has a strong influence on spattering. Qiu et al. [31] observed with high-speed imaging an increased number of ejections from the melt pool with increased thickness of the powder layer, from 20 μm to 100 μm. The present study observed, additionally, that larger portions of the build area are affected by spatter redeposition with increased layer thickness. This result suggests that mitigation of flaws caused by spatter redeposition on the powder bed is dependent on adjusting the gas flow according to the prevalence of spatters, rather than delimiting a fixed build-free area.

5. Conclusions

In this paper, spatters redeposited on the build area are located and quantified through in-situ monitoring and their presence is associated with large lack of fusion. LPBF of Hastelloy X was performed with parameters optimized to yield fully dense materials at three distinct layer thicknesses 80 μm, 120 μm and 150 μm. The main findings are summarized as follows:

- The spatter generated from LPBF processing of Hastelloy X is covered with chromium- and titanium-rich oxide layer of average thickness around 76 nm, has a bimodal size distribution with peaks around 30 μm and 90 μm, and consist of mostly spherical particles, but some agglomerates are consistently observed.
- Analysis of the fracture surface established a direct correlation between the presence of lack of fusion and spatter, unequivocally distinguished by the surface morphology and state of oxidation.
- Regions where spatter redeposits are detected contain large lack of fusion flaws.
- Specimens manufactured with identical process parameters can present significantly different flaw contents, depending on their positioning on the build plate.
- Redeposited spatters are preferentially detected on areas previously exposed by the laser, making the near-infrared long-exposure imaging particularly suitable for detecting spatter-induced stochastic lack of fusion.
- The spatial distribution of redeposited spatters on the powder bed is dependent on the scan strategy, as layer-wise differences on the spatial distribution transversally to the gas flow direction are verified when the direction of the laser path is rotated.
- The nominal layer thickness employed in the build process plays a major role in the prevalence and distribution of redeposited spatters. Spatters are verified to redeposit preferentially in the adjacencies of the gas outlet, however as the layer thickness increases, a larger number of redeposited spatters are detected, and across a larger portion of the build area. This result suggests that mitigation of flaws caused by spatter redeposition on the powder bed is dependent on adjusting the gas flow according to the prevalence of spatters and that laser beam attenuation, if not associated with redeposition of spatter on the powder bed, is not the determining mechanism of flaw generation.

CRediT authorship contribution statement

Claudia Schwerz: Conceptualization, Methodology, Software, Formal analysis, Investigation, Writing – original draft. **Ahmad Raza**: Investigation, Formal analysis, Writing – original draft. **Xiangyu Lei**: Investigation, Formal analysis, Writing – original draft. **Lars Nyborg**: Methodology, Writing – review & editing, Supervision, Funding acquisition. **Eduard Hryha**: Methodology, Writing – review & editing, Supervision, Funding acquisition. **Håkan Wirdelius**: Resources, Supervision.

Declaration of Competing Interest

The authors declare that they have no known competing financial interests or personal relationships that could have appeared to influence the work reported in this paper. Claudia Schwerz reports equipment, drugs, or supplies was provided by Electro Optical Systems.

Acknowledgements

This work was conducted within the framework of the Centre for Additive Manufacturing – Metal (CAM2), supported by the Swedish Governmental Agency of Innovation Systems (Vinnova), and of the project MANUELA - Additive Manufacturing using Metal Pilot Line, funded by European Union's Horizon 2020 Research and Innovation Programme under grant Agreement no. 820774. The authors would like to thank Electro Optical Systems Finland Oy for providing the feedstock powder utilized in this research.

References

[1] M. Grasso, B.M. Colosimo, Process defects and in situ monitoring methods in metal powder bed fusion: a review, Meas. Sci. Technol. 28 (2017), 044005, https://doi.org/10.1088/1361-6501/aa5c4f.
[2] A. Ladewig, G. Schlick, M. Fisser, V. Schulze, U. Glatzel, Influence of the shielding gas flow on the removal of process by-products in the selective laser melting process, Addit. Manuf. 10 (2016) 1–9, https://doi.org/10.1016/j.addma.2016.01.004.
[3] Z. Snow, A.R. Nassar, E.W. Reutzel, Invited review article: review of the formation and impact of flaws in powder bed fusion additive manufacturing, Addit. Manuf. 36 (2020), https://doi.org/10.1016/j.addma.2020.101457.
[4] Y. Liu, Y. Yang, S. Mai, D. Wang, C. Song, Investigation into spatter behavior during selective laser melting of AISI 316L stainless steel powder, Mater. Des. 87 (2015) 797–806, https://doi.org/10.1016/j.matdes.2015.08.086.
[5] S.A. Khairallah, A.T. Anderson, A. Rubenchik, W.E. King, Laser powder-bed fusion additive manufacturing: physics of complex melt flow and formation mechanisms of pores, spatter, and denudation zones, Acta Mater. 108 (2016) 36–45, https://doi.org/10.1016/j.actamat.2016.02.014.
[6] S. Ly, A.M. Rubenchik, S.A. Khairallah, G. Guss, M.J. Matthews, Metal vapor microjet controls material redistribution in laser powder bed fusion additive manufacturing, Sci. Rep. 7 (2017) 1–12, https://doi.org/10.1038/s41598-017-04237-z.
[7] P. Bidare, I. Bitharas, R.M. Ward, M.M. Attallah, A.J. Moore, Fluid and particle dynamics in laser powder bed fusion, Acta Mater. 142 (2018) 107–120, https://doi.org/10.1016/j.actamat.2017.09.051.
[8] Z.A. Young, Q. Guo, N.D. Parab, C. Zhao, M. Qu, L.I. Escano, K. Fezzaa, W. Everhart, T. Sun, L. Chen, Types of spatter and their features and formation mechanisms in laser powder bed fusion additive manufacturing process, Addit. Manuf. 36 (2020), 101438, https://doi.org/10.1016/j.addma.2020.101438.
[9] M. Simonelli, C. Tuck, N.T. Aboulkhair, I. Maskery, I. Ashcroft, R.D. Wildman, R. Hague, A study on the laser spatter and the oxidation reactions during selective laser melting of 316L stainless steel, Al-Si10-Mg, and Ti-6Al-4V, Metall. Mater. Trans. A Phys. Metall. Mater. Sci. 46 (2015) 3842–3851, https://doi.org/10.1007/s11661-015-2882-8.
[10] M. Lutter-Günther, M. Bröker, T. Mayer, S. Lizak, C. Seidel, G. Reinhart, Spatter formation during laser beam melting of AlSi10Mg and effects on powder quality, Procedia CIRP 74 (2018) 33–38, https://doi.org/10.1016/j.procir.2018.08.008.
[11] D. Wang, S. Wu, F. Fu, S. Mai, Y. Yang, Y. Liu, C. Song, Mechanisms and characteristics of spatter generation in SLM processing and its effect on the properties, Mater. Des. 117 (2017) 121–130, https://doi.org/10.1016/j.matdes.2016.12.060.
[12] R. Esmaeilizadeh, U. Ali, A. Keshavarzkermani, Y. Mahmoodkhani, E. Marzbanrad, E. Toyserkani, On the effect of spatter particles distribution on the quality of Hastelloy X parts made by laser powder-bed fusion additive manufacturing, J. Manuf. Process. 37 (2019) 11–20, https://doi.org/10.1016/j.jmapro.2018.11.012.
[13] A.R. Nassar, M.A. Gundermann, E.W. Reutzel, P. Guerrier, M.H. Krane, M. J. Weldon, Formation processes for large ejecta and interactions with melt pool formation in powder bed fusion additive manufacturing, Sci. Rep. 9 (2019) 1–11, https://doi.org/10.1038/s41598-019-41415-7.
[14] M. Tang, P.C. Pistorius, Oxides, porosity and fatigue performance of AlSi10Mg parts produced by selective laser melting, Int. J. Fatigue 94 (2017) 192–201, https://doi.org/10.1016/j.ijfatigue.2016.06.002.
[15] C.L.A. Leung, S. Marussi, R.C. Atwood, M. Towrie, P.J. Withers, P.D. Lee, In situ X-ray imaging of defect and molten pool dynamics in laser additive manufacturing, Nat. Commun. 9 (2018) 1–9, https://doi.org/10.1038/s41467-018-03734-7.
[16] Q. Guo, C. Zhao, L.I. Escano, Z. Young, L. Xiong, K. Fezzaa, W. Everhart, B. Brown, T. Sun, L. Chen, Transient dynamics of powder spattering in laser powder bed fusion additive manufacturing process revealed by in-situ high-speed high-energy x-ray imaging, Acta Mater. 151 (2018) 169–180, https://doi.org/10.1016/j.actamat.2018.03.036.
[17] G. Repossini, V. Laguzza, M. Grasso, B.M. Colosimo, On the use of spatter signature for in-situ monitoring of laser powder bed fusion, Addit. Manuf. 16 (2017) 35–48, https://doi.org/10.1016/j.addma.2017.05.004.
[18] Y. Zhang, J.Y.H. Fuh, D. Ye, G.S. Hong, In-situ monitoring of laser-based PBF via off-axis vision and image processing approaches, Addit. Manuf. 25 (2019) 263–274, https://doi.org/10.1016/j.addma.2018.10.020.
[19] G. Zenzinger, J. Bamberg, A.Ladewig, T. Hess, B. Henkel, W. Satzger, Process Monitoring of Additive Manufacturing by Using Optical Tomography, 2014. https://doi.org/10.1063/1.4914606.
[20] T. Lindeberg, Detecting salient blob-like image structures and their scales with a scale-space primal sketch: a method for focus-of-attention, Int. J. Comput. Vis. 11 (1993) 283–318, https://doi.org/10.1007/BF01469346.
[21] H. Kong, H.C. Akakin, S.E. Sarma, A generalized laplacian of Gaussian filter for blob detection and its applications, IEEE Trans. Cybern. 43 (2013) 1719–1733, https://doi.org/10.1109/TSMCB.2012.2228639.
[22] P.J. Shull, Nondestructive Evaluation – Theory, Techniques, and Applications, CRC Press, 2001, https://doi.org/10.1201/9780203911068.
[23] ISO 13320:2020 Particle Size Analysis—Laser Diffraction Methods, 2020.
[24] L. Nyborg, A. Nylund, I. Olefjord, Thickness determination of oxide layers on spherically-shaped metal powders by ESCA, Surf. Interface Anal. 12 (1988) 110–114, https://doi.org/10.1002/sia.740120209.
[25] C. Oikonomou, D. Nikas, E. Hryha, L. Nyborg, Evaluation of the thickness and roughness of homogeneous surface layers on spherical and irregular powder particles, Surf. Interface Anal. 46 (2014) 1028–1032, https://doi.org/10.1002/sia.5439.
[26] A. Bin Anwar, Q.C. Pham, Study of the spatter distribution on the powder bed during selective laser melting, Addit. Manuf. 22 (2018) 86–97, https://doi.org/10.1016/j.addma.2018.04.036.
[27] B. Ferrar, L. Mullen, E. Jones, R. Stamp, C.J. Sutcliffe, Gas flow effects on selective laser melting (SLM) manufacturing performance, J. Mater. Process. Technol. 212 (2012) 355–364, https://doi.org/10.1016/j.jmatprotec.2011.09.020.
[28] A. Masmoudi, R. Bolot, C. Coddet, Investigation of the laser-powder-atmosphere interaction zone during the selective laser melting process, J. Mater. Process. Technol. 225 (2015) 122–132, https://doi.org/10.1016/j.jmatprotec.2015.05.008.
[29] M. Taheri Andani, R. Dehghani, M.R. Karamooz-Ravari, R. Mirzaeifar, J. Ni, Spatter formation in selective laser melting process using multi-laser technology, Mater. Des. 131 (2017) 460–469, https://doi.org/10.1016/j.matdes.2017.06.040.
[30] M. Taheri Andani, R. Dehghani, M.R. Karamooz-Ravari, R. Mirzaeifar, J. Ni, A study on the effect of energy input on spatter particles creation during selective laser melting process, Addit. Manuf. 20 (2018) 33–43, https://doi.org/10.1016/j.addma.2017.12.009.
[31] C. Qiu, C. Panwisawas, M. Ward, H.C. Basoalto, J.W. Brooks, M.M. Attallah, On the role of melt flow into the surface structure and porosity development during selective laser melting, Acta Mater. 96 (2015) 72–79, https://doi.org/10.1016/j.actamat.2015.06.004.
[32] American Society for Metals, ASM Handbook, Volume 11, Failure Analysis and Prevention, 2002. http://books.google.com.hk/books?id=eC-Zt1J4oCgC.